CHINESE OPTICS LETTERS

Vol. xx, No. x | April 2024

Time-Resolved Photoluminescence: A Precision Tool for Shallow Trap Density Determination in Perovskite Films

Wei Chen (陈 威)[1,2], Yifeng Shi (史亦沣)[1], Pengxiang Wang (王鹏祥)[1], Guodong Zhang (张国栋)[1], Hu Wang (王 虎)[1], Yifan Zheng（郑毅帆）[1*], Yuchuan Shao（邵宇川）[1**]

[1] Key Laboratory of Materials for High-Power Laser, Shanghai Institute of Optics and Fine Mechanics, Chinese Academy of Sciences, Shanghai 201800, China

[2] School of Material Science and Technology, ShanghaiTech University, Shanghai 201210, China

[*] **Corresponding author:** yifanzheng@siom.ac.cn

[**] **Corresponding author:** shaoyuchuan@siom.ac.cn

Received Month X, XXXX | Accepted Month X, XXXX | Posted Online Month X, XXXX

Determining the trap density in the absorbing layer thin film of perovskite solar cells is a critically important task, as it directly influences the efficiency of the devices. Here, we proposed time-resolved photoluminescence (TRPL) as a non-destruction method to assess trap density. A model was constructed to investigate carrier recombination and transition in perovskite materials. The model was utilized for numerical calculations and successfully fitted TRPL signals of perovskite materials. Furthermore, a genetic algorithm was employed to optimize the parameters. Finally, statistical methods were applied to obtain the parameters associated with the trap states of the material. This approach facilitates the successful determination of trap densities for different samples with clear differentiation.

Keywords: perovskite solar cell, time-resolved photoluminescence, genetic algorithm, trap density, methylammonium lead triiodide.

DOI: xxxxxxx/COLxxxxxxx.

1. Introduction

In recent years, perovskite materials have garnered significant attention due to its potential to rival the efficiency of silicon-based solar cells[1–7]. Determining trap density is imperative in improving the quality of thin films, which is critical to enhancing the efficiency of solar cells[8–10]. Numerous techniques have been employed to quantify this parameter, such as transient capacitance, photoconductivity decay, and thermal admittance spectroscopy[11–13]. However, extracting parameters from photovoltaic measurements can be a complex process due to various factors that may affect the accuracy of the results, including the deactivation of excitons at the cathode, non-ohmic electrode contacts, filter effects, and pinhole defects in the photoactive layers[14]. In order to perform a quantitative analysis of traps, it is essential to introduce optical characterization strategy rather than electrical detection method. This non-destructive optical approach not only preserves the film's integrity but also enables monitoring of its quality prior to device fabrication. Notably, the optical method does not necessitate a specific sample area size, rendering it suitable for the characterization of large-area thin films. It can efficiently assess film quality by individually examining small regions, as well as perform a lattice-based inspection to evaluate the uniformity of the entire film, thereby maximizing its commercial value.

Time-resolved photoluminescence (TRPL) is an optical tool that researchers extensively use to study the carrier dynamics of various materials, including semiconductors, metallic oxides, two-dimensional nanomaterials, nanowires, and quantum wells[15–19]. Moreover, this technique has been widely used to assess the quality of perovskite materials. TRPL offers the flexibility to be performed under various excitation conditions, including different wavelengths, intensities, and temperatures. As a result, it has gained widespread usage in the field as a reliable tool for evaluating perovskite quality and identifying avenues for performance enhancement[20–23].

Generally, the information that can be directly extracted from TRPL images is fluorescence lifetime rather than trap density. The lifetime can be obtained by analyzing the fluorescence decay curve and performing a bi-exponential

fit,

$$I = A_1 e^{-\frac{t}{\tau_1}} + A_2 e^{-\frac{t}{\tau_2}} \quad (1)$$

, resulting in two fluorescence lifetimes, τ_1 and τ_2. Researchers typically assessed trap density indirectly by comparing τ_2, which is longer than τ_1, of different films. Because the longer τ_2 is considered to indicate a smaller proportion of non-radiative recombination, and thus a smaller trap density [24].

However, there are two issues here: a principal issue and a precision issue. In terms of the principal issue, τ_2 alone does not provide a straightforward indication of the magnitude of trap density. The two fluorescence lifetimes do not correspond one-to-one with the decay rates of carriers associated with different recombination paths; they are intrinsically coupled [25]. In addition, electrons captured by trap states could undergo transitions to the conduction band, increasing the likelihood of recombination with holes through band-to-band recombination, a process known as detrapping, which can extend the value of τ_2 and potentially complicate the determination of trap density. Concerning the precision issue, the presence of parameter adjustment space in bi-exponential fitting lacks a standardized method for selecting the most reliable set of parameters. As a result, the same curve can yield different interpretations, diminishing the method' s credibility. Therefore, it is necessary to reexamine the processing procedure of TRPL data to enable accurate quantification of defect parameters.

In this study, we addressed the principal concern by establishing corresponding models based on carrier recombination and transition mechanisms in perovskite materials. Furthermore, we introduced a genetic algorithm (GA) combined with statistical methods to address the precision issue [26]. The parameters obtained through this new fitting strategy are more accurate than conventional fitting results, as they represent the most probable values extracted from the distribution of collected data. Consequently, this innovative approach holds significant importance in the field of trap density engineering as it enables precise determination of trap density, optimization of device performance, and provides a more accurate and efficient method for assessing the quality of perovskite films.

2. Results and Discussion

2.1. Comparative Experiment

In this study, methylammonium lead triiodide ($MAPbI_3$) thin films were used as test samples, and anilinium hypophosphite (AHP) was used as an additive for film modification. Previous research has confirmed the effective improvement of film quality through this modification method [27]. Two types of film samples were prepared: a control group without AHP and a target group with AHP. Two randomly selected samples were taken from each group, labeled as Control 1 and 2 for the control group, and Target 1 and 2 for the target group. Their trap density of states (tDOS) was measured using thermal admittance spectroscopy (TAS) and the results are shown in Fig.1a. Since tDOS can be integrated to obtain trap density, we can infer from these results that the overall trap density of the devices decreased after the addition of AHP. Considering that the only difference in the device structure is the absorbing layer film, it can be concluded that the main reason for the decrease in trap density is the reduction in the trap density of the thin film [28].

Based on this premise, one sample was randomly selected from each group, and TRPL measurements were conducted under high and low excitation intensities. The results are shown in Fig.1b. After fitting the TRPL signals in Fig.1b using a bi-exponential fitting method, it was found that under low excitation conditions, the target sample had a shorter τ_2 (452.87 ns) compared to the control sample (639.75 ns), while under high excitation conditions, the target sample had a longer τ_2 (383.18 ns) compared to the control sample (365.43 ns). This indicates that the numerical value of τ_2 cannot be directly used as a basis for judging the trap density under a single excitation intensity.

Considering this phenomenon, we further explore and optimize the use of the TRPL method.

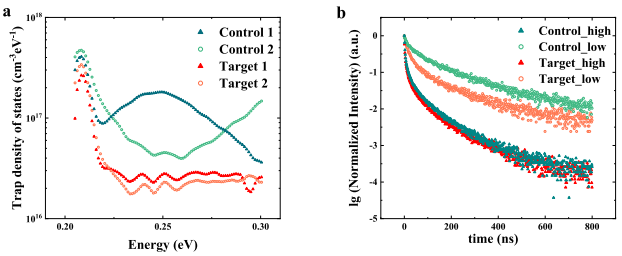

Fig. 1. Comparative experiment. (a) Trap density of states (tDOS) of the device obtained before and after addition. (b) Comparison of TRPL signals between the control group and the target group at different excitation light intensities .

2.2. TRPL Model

In the model established by Maiberg *et al.* in 2015, the transition rates derived from SRH theory are applied to a trap state located within a p-type semiconductor [29,30]. In order to represent it visually, the carriers' transition demonstrated by Eq.2 is illustrated in Fig.2a.

$$\begin{aligned} \frac{d}{dt}n &= G - R_{\mathrm{n}} + e_{\mathrm{e}} - e_{\mathrm{c}} \\ \frac{d}{dt}p &= G - R_{\mathrm{p}} + h_{\mathrm{e}} - h_{\mathrm{c}} \\ \frac{d}{dt}n_t &= e_{\mathrm{c}} - e_{\mathrm{e}} + h_{\mathrm{e}} - h_{\mathrm{c}} \end{aligned} \quad (2)$$

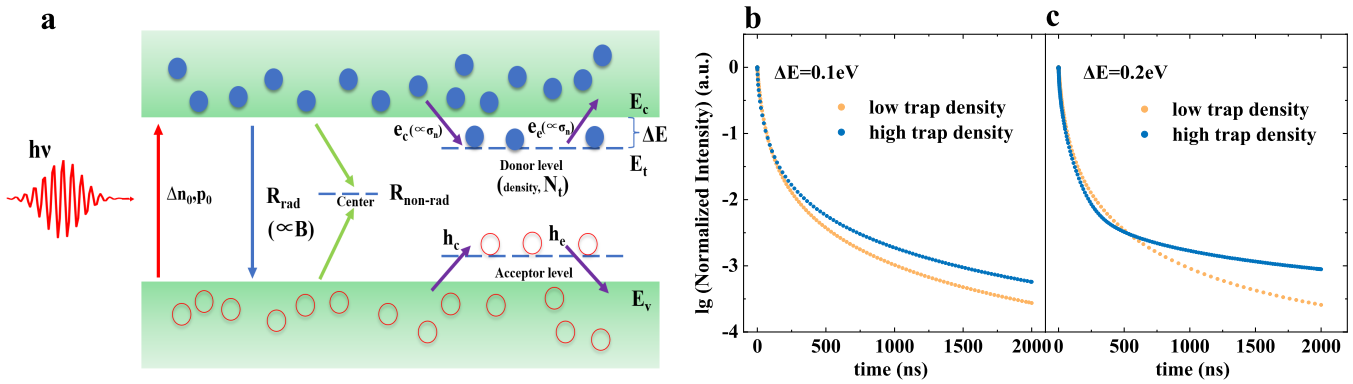

Fig. 2. Mechanism of carrier recombination and its TRPL simulation. (a) Scheme diagram of the original model of charge carrier trapping, detrapping, and recombination in $MAPbI_3$. Solid blue circles represent electrons, and hollow red circles represent holes. (b) Comparison of TRPL signals for different quality films with a trap depth of 0.1 eV. (c) Comparison of TRPL signals for different quality films with a trap depth of 0.2 eV .

Where G represents the generation rate, R denotes the radiative recombination rate, e_e signifies the electron emission rate, e_c stands for the electron capture rate, h_e indicates the hole emission rate and h_c refers to the hole capture rate.

In this study, we simplify the model by using p-doped $MAPbI_3$, which implies that the trap levels are primarily concentrated near the conduction band. For simplicity, we consider all potential wells as a single-level trap state, which we refer to as the trap distribution maximum. Therefore, we will focus on e_e, e_c, h_e, and h_c related to the potential well at the donor level. C e_c and h_c. By adopting this simplified approach, we aim to accurately capture the trapping dynamics and non-radiative processes that influence the film's overall performance. In TRPL experiments, the generation term should be zero, and carriers created by excitation can be incorporated into boundary conditions. The recombination terms $R_{n,p}$ are considered radiative terms based on our previous assumption. Subsequently, each term is expanded.

$$\begin{aligned}
\frac{d}{dt}n &= -B(np-n_0p_0)+\sigma_n v_n n^* n_t - \sigma_n v_n n\,(N_t-n_t)\\
\frac{d}{dt}p &= -B(np-n_0p_0)+\sigma_p v_p p^*\,(N_t-n_t) - \sigma_p v_p p n_t\\
\frac{d}{dt}n_t &= \sigma_n v_n n\,(N_t-n_t) - \sigma_n v_n n^* n_t\\
&\quad + \sigma_p v_p p^*\,(N_t-n_t) - \sigma_p v_p p n_t
\end{aligned} \tag{3}$$

We simplify these equations as follows:

$$\begin{aligned}
\frac{d}{dt}n &= -B(np-n_0p_0)+\sigma_n v_n n^* N_t f - \sigma_n v_n n N_t\,(1-f)\\
\frac{d}{dt}p &= -B(np-n_0p_0)+\sigma_p v_p p^* N_t\,(1-f) - \sigma_p v_p p N_t f\\
\frac{d}{dt}f &= \sigma_n v_n n\,(1-f) - \sigma_n v_n n^* f\\
&\quad + \sigma_p v_p p^*\,(1-f) - \sigma_p v_p p f
\end{aligned} \tag{4}$$

Where B represents the radiative recombination rate, N_t denotes the trap density, $\sigma_{n,p}$ signifies the capture cross-section, and $v_{n,p}$ indicates the thermal velocity of electrons and holes. Moreover, f represents the probability that a trap will contain an electron while n_t equals N_t multiplied by f. Furthermore, it is $n^* = N_c e^{-\frac{E_c-E_t}{kT}}$ the electron density and $p^* = N_v e^{-\frac{E_t-E_v}{kT}}$ the hole density if the Fermi-level lies at the trap level E_t, the parameter N_c is referred to as the effective density of states function in the conduction band, while N_v is known as the effective density of states functions in the valence band. Additionally, E_c represents the conduction band level, E_v describes the valance band level, and E_t illustrates the trap level. In the following, we define ΔE as $E_c - E_t$.

Next, we establish the boundary conditions for p-doped $MAPbI_3$,

$$\begin{aligned}
f(0) &= \frac{1}{1+\frac{1}{2}\exp\left(\frac{\frac{E_g}{2}-\Delta E-kT\ln\frac{n(0)}{n_i}}{kT}\right)}\\
n(0) &= n_0+\Delta n_0\\
p(0) &= p_0+\Delta n_0
\end{aligned} \tag{5}$$

Where E_g represents the band gap, ΔE denotes the trap depth, k is the Boltzmann constant, T is the temperature in Kelvin, n_i stands for intrinsic carrier concentration, and n_0,p_0 represent initial concentrations of electrons and holes respectively. Δn_0 and Δp_0 indicate generated concentrations of electrons and holes by excitation.

Additionally, Table 1 presents the fixed parameters utilized in the simulation. By incorporating these fixed parameters, we significantly enhance the accuracy and reliability of the fitting results.

The present model can be utilized for conducting simulation analysis. The parameters can be classified into two major groups, each of which can be further subdivided into two subgroups based on trap density. This classification

Table 1. Value of fixed parameters used in all simulations if not stated otherwise.

Fixed parameter	Value
Thermal velocity v_n,v_p	10^7 cm s^{-1} [30]
Effective density of states function in the conduction band N_c	2×10^{18} cm^{-3} [31]
Effective density of states function in the valence band N_v	3×10^{18} cm^{-3} [31]
Absorber bandgap E_g	1.55 eV [32]
Device temperature T	300K

facilitates a comprehensive analysis of TRPL performance across diverse parameter settings. The parameters for the main groups can be found in Table S1, where the arrow within the trap distribution maximum column (ΔE) distinguishes between the two parameter sets, providing clear differentiation.

Fig.2b clearly shows that when different trap depths are set, low-quality films exhibit distinct decay trends compared to high-quality films. To provide a quantitative explanation, we perform curve fitting on the plotted data in the figure:

$$I = -3.76 + 1.29e^{-\frac{t}{72.34}} + 2.44e^{-\frac{t}{853.41}} \quad \text{,for low trap density}$$
$$I = -3.42 + 1.20e^{-\frac{t}{59.54}} + 2.16e^{-\frac{t}{869.31}} \quad \text{,for high trap density} \tag{6}$$

It can be observed that the τ_2 extracted from the low trap density films is shorter than that of high trap density films. Similarly, we subjected data in Fig.2c to the same processing, obtaining the corresponding fitting equations.

$$I = -3.72 + 1.18e^{-\frac{t}{62.80}} + 2.52e^{-\frac{t}{745.73}} \quad \text{,for low trap density}$$
$$I = -3.07 + 1.60e^{-\frac{t}{81.24}} + 1.39e^{-\frac{t}{611.60}} \quad \text{,for high trap density} \tag{7}$$

In contrast to Eq.6, it is evident that in Eq.7, the τ_2 extracted from low trap density films is longer than that of high trap density films. Through this simulation, it is clear that the traditional method of determining lifetime may not accurately reflect the underlying quality factors, necessitating the development of alternative techniques for assessing sample quality.

2.3. Genetic Algorithm

In this work, when processing the TRPL signal obtained at a single excitation light intensity, we found that a single TRPL curve can be fitted with many different combinations of parameters. To address this issue, we simultaneously fitted three curves of a sample under different excitation intensities. To improve the fitting efficiency, we introduced a genetic algorithm to optimize the fitting process and constrain the parameter range.

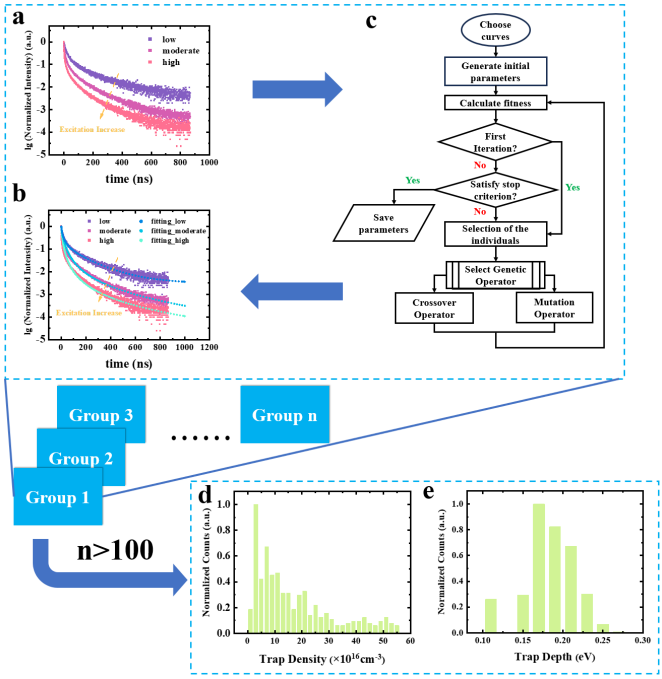

Fig. 3. Schematic diagram of the fitting process. (a) Original TRPL data of $MAPbI_3$ with different excitations. (b) Fitting curves of $MAPbI_3$ with different excitations. (c) The process of using genetic algorithm to find a reasonable combination of parameters. (d)-(e) The statistical distribution of (d) trap densities and (e) trap depths, values are extracted by hundreds of fitting processes and the number of these values falling within each interval is counted.

Fig.3a displays the TRPL signals of a sample at different excitation light intensities, which are computed through the fitting module depicted in Fig.3c. This module illustrates the process of fitting and parameter optimization using a GA. To achieve success with the TRPL fitting technique and GA, it is crucial to select the appropriate fitness function, and in each iteration, the coefficient of determination (R^2) is used to assess the fitness. After inputting the TRPL data, the parameter set in the model is initialized. It's worth noting that in the GA, a large number of parameter sets, referred to as individuals, are generated and their fitness is evaluated. In subsequent iterations, if the fitness exceeds a threshold, the individual is retained. If not, the optimal individual is selected for the next iteration, while the other individuals undergo crossover and mutation operations before entering the next iteration. Through this iterative process, a set of optimal parameter combinations is ultimately obtained. Fig.3b showcases the fitted curve generated by this set of parameters.

The process above is iterated multiple times, generating numerous parameter sets that can fit the three curves

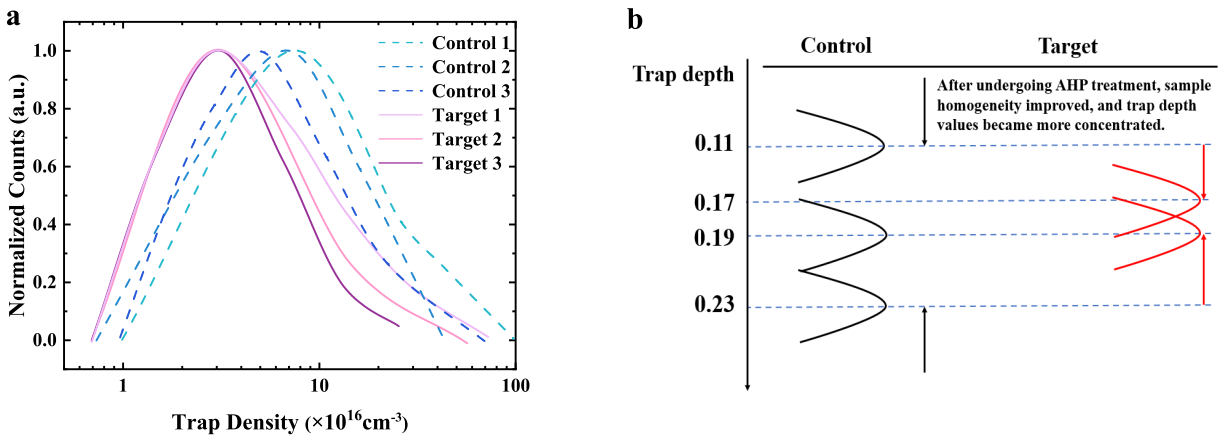

Fig. 4. Statistical distribution of the parameters. (a) Statistical distribution of trap density extracted from different signals. (b) Statistical distribution of trap depth extracted from different samples. The black curves on the graph represent the control group, whereas the red curves represent the target group.

simultaneously. While individual data points may exhibit randomness, a more extensive dataset demonstrates statistical patterns and converges to a specific range. By evaluating the peak of the distribution, we can effectively differentiate the quality disparity between different films.

2.4. Determination of Trap Density and Depth

The fitting process involves optimizing several parameters, including the maximum trap distribution (ΔE), trap density (N_t), electron capture cross-section (σ_n), radiative recombination rate (B), and incident intensity (Δn_0, Δp_0, where we represent intensity using the carrier density excited by the incident laser). The range of values for these parameters can be found in Table 2, which is a valuable reference for setting up the fitting process.

Table 2. Range of varied parameters used for fitting.

Fitting parameter	Range
Trap density N_t	$10^{15} \sim 10^{18}$ cm^{-3}
Trap distribution maximum ΔE	0.1∼0.4 eV
Electron capture cross-section σ_n	$10^{-17} \sim 10^{-15}$ cm^2
Radiative recombination rate B	$10^{-11} \sim 10^{-9}$ cm^{3}s^{-1}
Incident intensity Δn_0, Δp_0	$10^{16} \sim 10^{19}$ cm^{-3}

As shown in Fig.3d and 3e, after the iterative fitting process, we analyzed the large number of obtained parameter combinations. We calculated the distribution of the parameters within various intervals and extracted the statistical distributions of the trap density and trap depth. Subsequently, we visualized these distributions by creating a histogram.

Three samples were randomly selected from each of the control and target groups for testing. The control samples were labeled as Control 1, Control 2, and Control 3, while the target samples were labeled as Target 1, Target 2, and Target 3. TRPL tests were conducted on these samples under varying excitation intensity conditions, and the obtained signals were fitted using the fitting program above. Fig.4a shows the statistical distribution of trap densities obtained from the fitted results. The most probable trap densities for Target 1, Target 2, and Target 3 were all 3×10^{16} cm^{-3}, while for Control 1, Control 2, and Control 3, the most probable trap densities were 7.5×10^{16} cm^{-3}, 7×10^{16} cm^{-3}, and 5×10^{16} cm^{-3}, respectively, consistent with trap densities of existing literature on undoped $MAPbI_3$ films[33–35].

Moreover, according to the analysis of trap depth data in Fig.4b, it can be observed that the control group exhibits a relatively scattered distribution of trap depths, with a range of up to 0.12 eV. Based on the comprehensive analysis of the obtained parameters, we found two changes in trap density for the target group compared to the control group. Firstly, the overall trap density in the target group decreased, with a reduction ranging from 40% to 60% compared to the control group. Secondly, the values of trap density became more uniform, with the majority of trap density values distributed within a narrow range close to 3×10^{16} cm^{-3}. Additionally, there were two changes in trap depth for the target group relative to the control group. Firstly, the overall trap depth tended to be closer to the median value compared to the films before AHP modification. Secondly, the range of trap depths became narrower. In conclusion, the numerical results obtained through the TRPL method indicate that AHP treatment reduces the trap density of the thin film and improves its uniformity. This is consistent with previous literature reports and further confirms the feasibility of this method[27].

In order to validate the universality of this method, we applied it to process the TRPL signals of several other perovskite materials. The corresponding data can be found in Table S3.

From this point of view, TRPL can facilitate the multi-dimensional characterization of physical parameters germane to the film, which are pivotal in determining its overall properties. This method enables a comprehensive assessment of the relevant physical parameters to fully comprehend the film's properties.

3. Conclusion

This study effectively addressed the principal limitations of the fitting process through the formulation of a robust physical model. Moreover, we enhanced the precision of the fitting process by integrating advanced statistical methodologies. By employing iterative fitting, we successfully identified a prominent peak in the trap density distribution curve, signifying the most probable trap density value. Leveraging these advancements, we accurately quantified the trap density of diverse samples and achieved satisfactory outcomes. Additionally, the observed variation in decay rates among the undoped films can be attributed to the trapping-detrapping phenomenon, which is associated with a broad range of trap depths. In summary, this innovative approach holds significant implications for trap density engineering as it enables precise determination of trap density, optimization of device performance, and provides a more accurate and efficient means of assessing the quality of perovskite films.

4. Experimental Section

4.1. Materials

We procured the following materials: Poly(bis(4-phenyl)(2,4,6-trimethylphenyl)amine) (PTAA, Mn 7,000–10,000), bathocuproine (BCP), lead (II) iodide (PbI_2, 99.99% trace metals), Methylammonium iodide (MAI), and Methylammonium chloride (MACl) from Xi' an Polymer Light Technology Corp. N, N-dimethylformamide (DMF, 99.9%), Dimethyl sulfoxide (DMSO, 99.9%), 2-methoxyethanol (2-ME, 99.8%), chlorobenzene (CB, 99.8%), anilinium hypophosphite (AHP), and L-α-phosphatidylcholine (L-α-PC) from Sigma-Aldrich. Additionally, we purchased C60 from Advanced Election Technology CO., Ltd and ITO-coated glass substrates (15 $\Omega \cdot \mathrm{sq}^{-1}$) from South China Science & Technology Co. Ltd. All materials were utilized without further purification, and copper for thermal evaporation was sourced from ZhongNuo Advanced Material (Beijing) Technology Co., Ltd.

4.2. Precursor Preparation

For the PTAA solution, PTAA powder was dissolved in CB at a concentration of 6 mg/ml. The precursor solutions for $MAPbI_3$, with a concentration of 2.0M, were prepared by dissolving MAI and PbI_2 in 2-ME and stirring overnight. Prior to blade coating, these precursor solutions were diluted to 1.1M. To create the pristine films, additives such as L-α-PC (0.4 mg/ml), MACl (0.2 mg/ml), and DMSO (2.8% v/v) were introduced into the precursor solution. In the case of the optimized films, an AHP solution (20 mg/ml) was prepared by dissolving AHP in 2-ME and added to the precursor solution as an additional additive (4% v/v).

4.3. TRPL

Time-resolved photoluminescence (TRPL) measurements of perovskite samples were conducted using a 405-nm picosecond pulsed diode laser in conjunction with a laser-scanned fluorescence lifetime/intensity imaging system (FLRM300, Time-Tech Spectra, LLC). TRPL lifetime measurements were performed using a time-correlated single photon counter setup with a laser repetition rate of 0.5 MHz. The samples were tested at room temperature, and a laser with a power of 1.69 μW was used. Two optical filters were employed to obtain three different orders of incident intensity, resulting in intensity values of 1.69 μW, 0.169 μW, and 0.0169 μW, respectively.

4.4. tDOS

During the tDOS measurement, a fixed DC bias of 0 V, accompanied by an AC bias amplitude of 20mV. The frequency dependence of the capacitance was then recorded within the range of 1 kHz to 5 MHz. The tDOS ($N_T(E_\omega)$) is calculated from C-f measurements using an equation $N_T(E_\omega) = -\frac{1}{qkT}\frac{\omega dC}{d\omega}\frac{V_{bi}}{W}$. The depletion width ($W$) and built-in potential (V_{bi}) are derived from the Mott-Schottky analysis of C-V measurements. The calculation of the demarcation energy E_ω involves the use of an equation $E_\omega = kT\ln\left(\frac{\omega_0}{\omega}\right)$, wherein ω_0 represents the angular frequency of an attempt-to-escape event, which is equal to $2\pi v_0 T^2$.

Supplementary Information

Supplementary Information is available from the Optica Publishing Group or from the author.

Acknowledgments

This work is supported by the National Natural Science Foundation of China (62104234 and 52103279), the Shanghai Sailing Program (21YF1454000).

References

1. M. Li, Y.-G. Yang, Z.-K. Wang, T. Kang, Q. Wang, S.-H. Turren-Cruz, X.-Y. Gao, C.-S. Hsu, L.-S. Liao, and A. Abate, "Perovskite grains embraced in a soft fullerene network make highly efficient flexible solar cells with superior mechanical stability," *Adv. Mater.*, vol. 31, no. 25, p. 1901519, 2019.
2. Y. Chen, X. Zuo, Y. He, F. Qian, S. Zuo, Y. Zhang, L. Liang, Z. Chen, K. Zhao, Z. Liu *et al.*, "Dual passivation of perovskite and SnO2 for high-efficiency MAPbI3 perovskite solar cells," *Adv. Sci.*, vol. 8, no. 5, p. 2001466, 2021.
3. Z. Chen, B. Turedi, A. Y. Alsalloum, C. Yang, X. Zheng, I. Gereige, A. AlSaggaf, O. F. Mohammed, and O. M. Bakr, "Single-crystal mapbi3 perovskite solar cells exceeding 21% power conversion efficiency," *ACS Energy Lett.*, vol. 4, no. 6, pp. 1258–1259, 2019.
4. N. Li, A. Feng, X. Guo, J. Wu, S. Xie, Q. Lin, X. Jiang, Y. Liu, Z. Chen, and X. Tao, "Engineering the hole extraction interface enables single-crystal mapbi3 perovskite solar cells with efficiency exceeding 22% and superior indoor response," *Adv. Energy Mater.*, vol. 12, no. 7, p. 2103241, 2022.
5. J. Chang, H. Zhu, B. Li, F. H. Isikgor, Y. Hao, Q. Xu, and J. Ouyang, "Boosting the performance of planar heterojunction perovskite solar cell by controlling the precursor purity of perovskite materials," *J. Mater. Chem.A*, vol. 4, no. 3, pp. 887–893, 2016.
6. E. A. Alharbi, A. Krishna, T. P. Baumeler, M. Dankl, G. C. Fish, F. Eickemeyer, O. Ouellette, P. Ahlawat, V. Škorjanc, E. John *et al.*, "Methylammonium triiodide for defect engineering of high-efficiency perovskite solar cells," *ACS Energy Lett.*, vol. 6, no. 10, pp. 3650–3660, 2021.
7. P. Chen, Y. Bai, S. Wang, M. Lyu, J.-H. Yun, and L. Wang, "In situ growth of 2d perovskite capping layer for stable and efficient perovskite solar cells," *Adv. Funct. Mater.*, vol. 28, no. 17, p. 1706923, 2018.
8. J. Jiang, Z. Jin, F. Gao, J. Sun, Q. Wang, and S. Liu, "Cspbcl3-driven low-trap-density perovskite grain growth for> 20% solar cell efficiency," *Adv. Sci.*, vol. 5, no. 7, p. 1800474, 2018.
9. D. Bai, J. Zhang, Z. Jin, H. Bian, K. Wang, H. Wang, L. Liang, Q. Wang, and S. F. Liu, "Interstitial mn2+-driven high-aspect-ratio grain growth for low-trap-density microcrystalline films for record efficiency cspbi2br solar cells," *ACS Energy Lett.*, vol. 3, no. 4, pp. 970–978, 2018.
10. F. Cai, Y. Yan, J. Yao, P. Wang, H. Wang, R. S. Gurney, D. Liu, and T. Wang, "Ionic additive engineering toward high-efficiency perovskite solar cells with reduced grain boundaries and trap density," *Adv. Funct. Mater.*, vol. 28, no. 34, p. 1801985, 2018.
11. Y. C. Choi, D. U. Lee, J. H. Noh, E. K. Kim, and S. I. Seok, "Highly improved sb2s3 sensitized-inorganic–organic heterojunction solar cells and quantification of traps by deep-level transient spectroscopy," *Adv. Funct. Mater.*, vol. 24, no. 23, pp. 3587–3592, 2014.
12. K. Lauer, A. Laades, H. Übensee, H. Metzner, and A. Lawerenz, "Detailed analysis of the microwave-detected photoconductance decay in crystalline silicon," *J. Appl. Phys.*, vol. 104, no. 10, 2008.
13. S. Wang, P. Kaienburg, B. Klingebiel, D. Schillings, and T. Kirchartz, "Understanding thermal admittance spectroscopy in low-mobility semiconductors," *The Journal of Physical Chemistry C*, vol. 122, no. 18, pp. 9795–9803, 2018.
14. J. E. Kroeze, T. J. Savenije, and J. M. Warman, "Electrodeless determination of the trap density, decay kinetics, and charge separation efficiency of dye-sensitized nanocrystalline tio2," *J. Am. Chem. Soc.*, vol. 126, no. 24, pp. 7608–7618, 2004.
15. K. Fujihara, S. Izumi, T. Ohno, and M. Matsumura, "Time-resolved photoluminescence of particulate tio2 photocatalysts suspended in aqueous solutions," *Journal of Photochemistry and Photobiology A: Chemistry*, vol. 132, no. 1-2, pp. 99–104, 2000.
16. A. Gorgis, T. Flissikowski, O. Brandt, C. Chèze, L. Geelhaar, H. Riechert, and H. Grahn, "Time-resolved photoluminescence spectroscopy of individual gan nanowires," *Physical review B*, vol. 86, no. 4, p. 041302, 2012.
17. P. Lefebvre, J. Allègre, B. Gil, H. Mathieu, N. Grandjean, M. Leroux, J. Massies, and P. Bigenwald, "Time-resolved photoluminescence as a probe of internal electric fields in gan-(gaal) n quantum wells," *Phys. Rev. B*, vol. 59, no. 23, p. 15363, 1999.
18. J. Ryan, R. Taylor, A. Turberfield, A. Maciel, J. Worlock, A. Gossard, and W. Wiegmann, "Time-resolved photoluminescence of two-dimensional hot carriers in gaas-algaas heterostructures," *Physical review letters*, vol. 53, no. 19, p. 1841, 1984.
19. J. Stathis and M. Kastner, "Time-resolved photoluminescence in amorphous silicon dioxide," *Phys. Rev. B*, vol. 35, no. 6, p. 2972, 1987.
20. J. Qin, X.-K. Liu, C. Yin, and F. Gao, "Carrier dynamics and evaluation of lasing actions in halide perovskites," *Trends in Chemistry*, vol. 3, no. 1, pp. 34–46, 2021.
21. Y. Yamada, M. Endo, A. Wakamiya, and Y. Kanemitsu, "Spontaneous defect annihilation in ch3nh3pbi3 thin films at room temperature revealed by time-resolved photoluminescence spectroscopy," *The journal of physical chemistry letters*, vol. 6, no. 3, pp. 482–486, 2015.
22. A. A. Baloch, F. H. Alharbi, G. Grancini, M. I. Hossain, M. K. Nazeeruddin, and N. Tabet, "Analysis of photocarrier dynamics at interfaces in perovskite solar cells by time-resolved photoluminescence," *The Journal of Physical Chemistry C*, vol. 122, no. 47, pp. 26 805–26 815, 2018.
23. Y. Yamada, T. Nakamura, M. Endo, A. Wakamiya, and Y. Kanemitsu, "Photocarrier recombination dynamics in perovskite ch3nh3pbi3 for solar cell applications," *J. Am. Chem. Soc.*, vol. 136, no. 33, pp. 11 610–11 613, 2014.
24. T. Du, J. Kim, J. Ngiam, S. Xu, P. R. Barnes, J. R. Durrant, and M. A. McLachlan, "Elucidating the origins of subgap tail states and open-circuit voltage in methylammonium lead triiodide perovskite solar cells," *Adv. Funct. Mater.*, vol. 28, no. 32, p. 1801808, 2018.
25. J. M. Ball and A. Petrozza, "Defects in perovskite-halides and their effects in solar cells," *Nat. Energy*, vol. 1, no. 11, pp. 1–13, 2016.
26. S. Mirjalili and S. Mirjalili, "Genetic algorithm," *Evolutionary Algorithms and Neural Networks: Theory and Applications*, pp. 43–55, 2019.
27. Y. Shi, Y. Zheng, X. Xiao, P. Wang, G. Zhang, Q. Li, G. Zhang, and Y. Shao, "Vertical grain-shape engineering for high-efficiency and stable perovskite solar cells," *Cell Reports Physical Science*, vol. 4, no. 11, 2023.
28. J. Zhou, D. He, Y. Li, F. Huang, J. Zhang, C. Zhang, Y. Yuan, Y. Lin, C. Wang, and F. Zhao, "Reducing trap density in organic solar cells via extending the fused ring donor unit of an a–d–a-type nonfullerene acceptor for over 17% efficiency," *Advanced Materials*, vol. 35, no. 3, 12 2022.
29. W. Shockley and W. Read Jr, "Statistics of the recombinations of holes and electrons," *Physical review*, vol. 87, no. 5, p. 835, 1952.
30. M. Maiberg, T. Hölscher, S. Zahedi-Azad, and R. Scheer, "Theoretical study of time-resolved luminescence in semiconductors. iii. trap states in the band gap," *J. Appl. Phys.*, vol. 118, no. 10, 2015.
31. B. Olyaeefar, S. Ahmadi-Kandjani, and A. Asgari, "Bulk and interface recombination in planar lead halide perovskite solar cells: A drift-diffusion study," *Physica E: Low-dimensional Systems and Nanostructures*, vol. 94, pp. 118–122, 10 2017.
32. A. M. A. Leguy, P. Azarhoosh, M. I. Alonso, M. Campoy-Quiles, O. J. Weber, J. Yao, D. Bryant, M. T. Weller, J. Nelson, A. Walsh, M. van Schilfgaarde, and P. R. F. Barnes,

"Experimental and theoretical optical properties of methylammonium lead halide perovskites," *Nanoscale*, vol. 8, no. 12, pp. 6317–6327, 2016.

33. G. Feng, P. Zeng, X. Liu, Y. Zhang, Y. Wang, Q. Zhang, S. Liu, and M. Liu, "A realistic model of temperature dependent carrier diffusion constant in mapbi3 films," *Appl. Surf. Sci.*, vol. 606, p. 154908, 2022.
34. G. Xing, N. Mathews, S. S. Lim, N. Yantara, X. Liu, D. Sabba, M. Grätzel, S. Mhaisalkar, and T. C. Sum, "Low-temperature solution-processed wavelength-tunable perovskites for lasing," *Nature materials*, vol. 13, no. 5, pp. 476–480, 2014.
35. S. Draguta, S. Thakur, Y. V. Morozov, Y. Wang, J. S. Manser, P. V. Kamat, and M. Kuno, "Spatially non-uniform trap state densities in solution-processed hybrid perovskite thin films," *The journal of physical chemistry letters*, vol. 7, no. 4, pp. 715–721, 2016.